

# A Secure Full-Duplex Wireless Circulator enabled by Non-Reciprocal Beyond-Diagonal RIS

Ziang Liu, and Bruno Clerckx, *Fellow, IEEE*

**Abstract**—Beyond-diagonal reconfigurable intelligent surface (BD-RIS) has arisen as a promising technology for enhancing wireless communication systems by enabling flexible and intelligent wave manipulation. This is achieved through the interconnections among the ports of the impedance network, enabling wave reconfiguration when they flow through the surface. Thus, the output wave at one port depends on waves impinging on neighboring ports, allowing non-local control of both phase and magnitude. Non-reciprocal (NR)-BD-RIS further enhances this capability by breaking circuit reciprocity and, consequently, channel reciprocity. This feature potentially benefits communication among non-aligned transceivers. This paper introduces a novel application of NR-BD-RIS in full-duplex (FD) wireless circulators, where multiple FD devices communicate via an NR-BD-RIS. This system is particularly beneficial for secure transmission, as it enforces one-way communication among FD devices, suppresses signal from all other users, and thus prevents eavesdropping. In addition, a physics-compliant system model is considered by incorporating structural scattering, also known as specular reflection. By accounting for this effect, the advantages of NR-BD-RIS are further validated. Specifically, we formulate an all-user sum-rate maximization problem and propose an iterative optimization algorithm that employs block coordinate descent (BCD) and penalty dual decomposition (PDD) methods. Numerical evaluations illustrate that NR-BD-RIS consistently outperforms reciprocal (R)-BD-RIS and conventional diagonal (D)-RIS in terms of sum-rate performance, particularly when more than two impinging and reflection directions need to be supported. By analyzing the power of signals from all other users and the beampatterns, we show that secure transmission can be achieved.

**Index Terms**—BD-RIS, eavesdropping, FD wireless circulator, non-reciprocity, structural scattering, secure transmission

## I. INTRODUCTION

Reconfigurable intelligent surface (RIS) has emerged as a promising technique for future wireless communications [1]. It has gained substantial interest in both academic research and the wireless industry due to its capability to intelligently manipulate electromagnetic wave propagation, thereby improving energy and spectrum efficiency [2]–[4]. RIS consists of a planar array of low-cost, energy-efficient passive reflecting elements with controllable phases. This enables the adjustment of incident, reflected, refracted, and scattered signals, facilitating the optimization of the propagation environment to enhance received signal power, sum-rate [5], and energy efficiency [3] in wireless systems. On the industrial front, RIS-related technologies, such as network-controlled repeaters (NCRs), have been introduced in the 3rd Generation Partnership Project

(3GPP)’s Release-18 to enhance spectral efficiency [6]. Concurrently, with the increasing number of wireless devices and dynamic channel environments, physical layer (PHY) security has become a critical concern. Recent studies have investigated the potential of RIS to enable secure communication and against jamming and eavesdropping attacks [7], [8].

A key limitation of conventional RISs [2]–[5], [9] is their inability to control the magnitude of impinging waves, as they can only adjust the phase. This restriction reduces the RIS’s effectiveness in passive beamforming and electromagnetic wave manipulation. The reason for this is that, in theory, the RIS is equivalent to an array of scattering elements connected to a reconfigurable impedance network [10]–[12]. In conventional diagonal RIS (D-RIS), each port of the impedance network is grounded via its impedance component, resulting in a single-connected structure. The resulting scattering matrix is diagonal, leading to the term D-RIS. To address this limitation and enable control over both the phase and magnitude of impinging waves, [10], [11] developed beyond-diagonal RIS (BD-RIS). In BD-RIS, the ports of the impedance network are interconnected, allowing waves to propagate across the surface and providing greater flexibility for analog-domain wave manipulation. If all ports are interconnected, it is referred to as fully-connected BD-RIS [10], characterized by a full scattering matrix that offers maximum control over wave manipulation at the expense of increased hardware complexity. To trade off flexibility and hardware complexity, group-connected RIS architectures have been designed, where ports are grouped, and all ports within a group are interconnected. The scattering matrix in this case is block diagonal, offering more flexibility than D-RIS while being less complex than fully-connected RIS. To further optimize the balance between performance and hardware complexity, [13], [14] designed tree- and forest-connected structures and their performance-hardware complexity Pareto frontier is analyzed. These architectures enhance communication performance compared to conventional D-RIS. For example, in [15], [16], closed-form solutions are used to maximize received power and capacity, demonstrating the superior performance of BD-RIS.

Losslessness and reciprocity are two commonly assumed properties of the reconfigurable impedance network in BD-RIS, as in most existing works [10], [11], [13]–[16]. Losslessness ensures that the network does not dissipate energy, meaning the power of the reflected waves equals that of the incident waves. This property is mathematically represented by the scattering matrix being unitary [12]. Reciprocity implies that the impedance between any two ports is symmetric, *i.e.*, the impedance from port  $i$  to port  $j$  is identical to

Z. Liu, and B. Clerckx are with the Communications & Signal Processing (CSP) Group at the Dept. of Electrical and Electronic Engg., Imperial College London, SW7 2AZ, UK. (e-mails: {ziang.liu20, b.clerckx}@imperial.ac.uk).

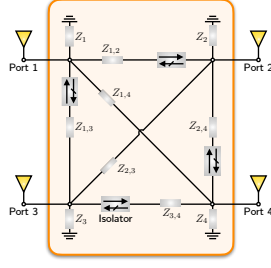


Fig. 1. Illustration of a 4-port non-reciprocal BD-RIS (NR-BD-RIS) hardware implementation [26].

that from port  $j$  to port  $i$ . This is mathematically described by the scattering matrix being symmetric [12]. Reciprocal BD-RIS (R-BD-RIS) has been extensively studied in prior works [10], [13]–[16]. In fact, a new degree of freedom for manipulating the electromagnetic environment can be achieved by breaking the reciprocity of the impedance network. Thus, the symmetric constraint on the scattering matrix can be relaxed, leading to a non-reciprocal BD-RIS (NR-BD-RIS). Non-reciprocity can be realized by integrating non-reciprocal components such as radio isolators (cf. Fig. 1), circulators, and radio frequency couplers [12]. Additionally, [17] proposed using switches based on RF micro-electromechanical systems (MEMS) [18] to realize a non-diagonal phase shift matrix. Metasurfaces have also been explored for achieving non-reciprocity [19]–[22]. These studies indicate the feasibility of hardware implementation of NR-BD-RIS. Non-reciprocity has been leveraged in some works to enhance communication system performance. For example, [17] demonstrated that a non-diagonal phase shift matrix can maximize channel gain. Similarly, [23] showed that a non-reciprocal scattering matrix can achieve spatial selectivity, mitigating interference from specific directions. Applications of NR-BD-RIS in secure communications and channel reciprocity attacks (CRACK) have been explored in [24], [25], respectively. Despite these advancements, the unique benefits of NR-BD-RIS as an enabler of new use cases not achievable with conventional D-RIS remain unexplored. This motivates further investigation into its potential for improving wireless communication systems.

Recent studies have demonstrated the benefits of NR-BD-RIS in full-duplex (FD) wireless communication systems. For instance, [27] theoretically shows that non-reciprocity improves received power for non-aligned downlink and uplink users in single-antenna FD systems, outperforming the performance of R-BD-RIS and D-RIS. Furthermore, [28] extends this analysis to a more general FD case, where a base station (BS) with multiple antennas transmits data to multiple downlink and uplink users. The findings reveal that NR-BD-RIS achieves higher sum-rate performance, especially when downlink and uplink users are non-aligned. Building on these studies, we propose a novel NR-BD-RIS-enabled secure wireless circulator, which incorporates both direct and reflected links and leverages the ability of NR-BD-RIS to break channel reciprocity. As illustrated in Fig. 2(a), the NR-BD-RIS can support multiple directions, effectively suppress interference from unwanted FD devices and enforce one-way

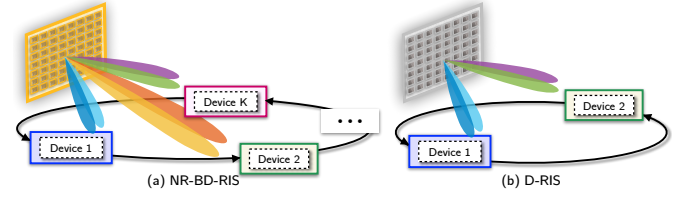


Fig. 2. A full-duplex (FD) wireless circulator enabled by (a) non-reciprocal BD-RIS (NR-BD-RIS). All FD devices communicate in one direction. (b) The conventional D-RIS can only support two non-aligned FD devices, which is not a wireless circulator.

secure communication. In contrast, the conventional D-RIS, as shown in Fig. 2(b), is limited to supporting only two non-aligned FD devices, making it impossible for enabling one-way communication among multiple FD devices. This one-way manner is particularly beneficial for physical layer security, as the user can only receive information from the previous user, preventing eavesdropping by other users.

**Contributions and Overview of Results.** The contributions are summarized as follows:

- We formulate a novel system model for the NR-BD-RIS-enabled secure FD wireless circulator in Fig. 3, where multiple FD users communicate via NR-BD-RIS and signals are transmitted in one direction. The signals from other FD users (*i.e.*, multi-user (MU) interference) are suppressed, which prevents eavesdropping. Each FD user is equipped with multiple antennas for simultaneous transmission and reception. The model accounts for self-interference, loop interference, and multi-user interference. Both direct and reflected channels are included to illustrate the advantages of the NR-BD-RIS.
- Unlike existing studies that neglect structural scattering, which represents specular reflection caused by the BD-RIS when inactive, we adopt a physics-compliant model that incorporates structural scattering. This model effectively demonstrates the consistent superiority of NR-BD-RIS over R-BD-RIS and D-RIS in terms of sum-rate performance.
- We formulate an all-user sum-rate maximization problem for the NR-BD-RIS-enabled FD wireless circulator. The problem involves optimizing precoders, combiners of FD users, and the scattering matrix of the BD-RIS, using an iterative optimization approach. Specifically, a block coordinate descent (BCD) framework is adopted to iteratively optimize all variables, while the scattering matrix is optimized using the penalty dual decomposition (PDD) method. Compared to [28], this approach is designed for the FD wireless circulator scenario, incorporates all-user sum-rate maximization, and effectively handles symmetry, asymmetry, and diagonality constraints.
- We demonstrate the unique benefit of NR-BD-RIS in effectively supporting more than two impinging and reflecting directions, which cannot be achieved by R-BD-RIS and conventional D-RIS. This unique feature enables the secure FD wireless circulator, facilitating one-way communication among multiple FD users. This benefit is validated through simulation results, which show that NR-BD-RIS

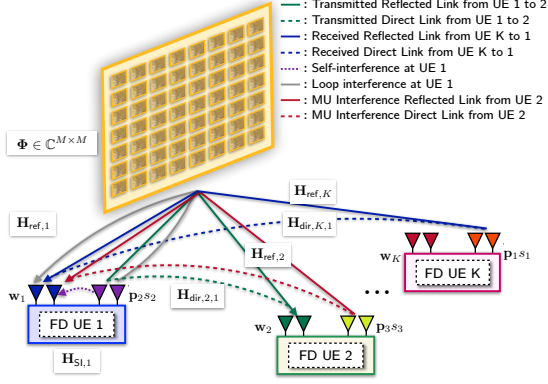


Fig. 3. The system model of NR-BD-RIS enabled FD wireless circulator.

consistently outperforms R-BD-RIS and D-RIS in terms of all-user sum-rate performance. This performance gain is attributed to the additional degree of freedom provided by non-reciprocity, which breaks channel reciprocity. The performance gain of NR-BD-RIS increases with the number of RIS elements, the group size of the BD-RIS, the number of antennas at each FD user, and the number of FD users. Additionally, structural scattering enhances sum-rate performance by increasing channel gain. The power of signals from other FD users and the beampatterns are analyzed to demonstrate the secure transmission capability of the proposed system.

**Organization of This Paper.** The system model is described in Section II. Based on it, we formulate the weighted all-user sum-rate maximization problem in Section III. Then, the optimization problem is transformed into a more tractable form. Subsequently, the proposed solution algorithm is presented in Section IV. In this section, the convergence and computational complexity are analyzed. The numerical evaluation is provided in Section V. We summarize the paper in Section VI.

**Notation.** The sets of binary, integer, real, and complex numbers are denoted as  $\mathbb{B}$ ,  $\mathbb{Z}$ ,  $\mathbb{R}$ , and  $\mathbb{C}$ , respectively. Bold uppercase letters represent matrices, bold lowercase letters denote vectors, and scalars are written in regular font. The real part of a complex number is expressed as  $\text{Re}(\cdot)$ . For a matrix  $\mathbf{X}$ , its complex conjugate, transpose, Hermitian transpose, and inverse are represented by  $\mathbf{X}^*$ ,  $\mathbf{X}^\top$ ,  $\mathbf{X}^H$ , and  $\mathbf{X}^{-1}$ , respectively. The element located at the  $i^{\text{th}}$  row and  $j^{\text{th}}$  column of  $\mathbf{X}$  is denoted as  $\mathbf{X}(i, j)$ . The identity matrix and the zero matrix are denoted by  $\mathbf{I}$  and  $\mathbf{0}$ , respectively. The operations of vectorization, diagonal matrix, block diagonal matrix, trace operation, and Kronecker product are denoted by  $\text{vec}(\cdot)$ ,  $\text{diag}(\cdot)$ ,  $\text{blkdiag}(\cdot)$ ,  $\text{Tr}(\cdot)$ , and  $\otimes$ , respectively.

## II. SYSTEM MODEL

As illustrated in Fig. 3, a secure FD wireless circulator is enabled by an  $M$ -element RIS. In this setup, all users operate in FD mode, allowing simultaneous transmission and reception. Each FD user is equipped with  $N_t$  transmit (TX) antennas and  $N_r$  receive (RX) antennas, with  $N_t = N_r = N$  for simplicity. The FD users are indexed by  $\mathcal{K} = \{1, \dots, K\}$ .

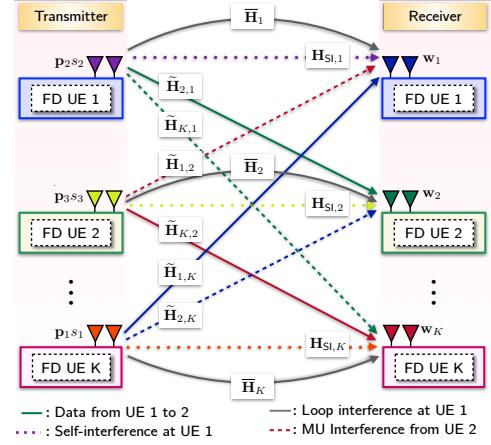


Fig. 4. Effective channels in the NR-BD-RIS enabled FD wireless circulator.

The following assumptions are made: *i*) Each FD user has perfect instantaneous channel state information (CSI). The CSI is acquired using BD-RIS channel estimation techniques [29]. *ii*) The  $(k-1)^{\text{th}}$  FD user transmits data to the  $k^{\text{th}}$  FD user. For  $k = K$ , the  $K^{\text{th}}$  FD user transmits to the  $1^{\text{st}}$  FD user, as depicted in Fig. 3. Therefore, the FD users are connected in a circular manner, allowing signals to propagate in one direction. This configuration is referred to as a wireless circulator. We use  $\Phi \in \mathbb{C}^{M \times M}$  to represent the scattering matrix of the BD-RIS. In the case of a group-connected BD-RIS, the group size is denoted as  $M_g$ , and the total number of groups is  $G = M/M_g$ . The group-connected BD-RIS is expressed as  $\Phi = \text{blkdiag}(\Phi_1, \dots, \Phi_G)$ . Notably, the D-RIS and fully-connected BD-RIS are special cases where  $G = M$  and  $G = 1$ , respectively.

Consider the  $(k-1)^{\text{th}}$  FD user as an example. During data transmission, the FD user applies the precoding matrix  $\mathbf{p}_k \in \mathbb{C}^N$  to the transmit symbol  $s_k$ , which is intended for the  $k^{\text{th}}$  FD user. Subsequently, the symbol is processed in baseband and up-converted. The resulting signal is sent via  $N$  antennas and propagates through both the direct and reflected paths. At  $k^{\text{th}}$  FD user, received signals are processed using the combiner  $\mathbf{w}_k \in \mathbb{C}^N$ . Let  $\mathbf{P} \triangleq [\mathbf{p}_1, \dots, \mathbf{p}_K] \in \mathbb{C}^{N \times K}$  and  $\mathbf{W} \triangleq [\mathbf{w}_1, \dots, \mathbf{w}_K] \in \mathbb{C}^{N \times K}$  represent the precoders and combiners for all  $K$  FD users. Note that the transpose operator  $(\cdot)^\top$  is used in channel-related expressions instead of the Hermitian operator  $(\cdot)^H$  to more accurately model channel reciprocity. As illustrated in Fig. 4, the effective channels are defined as  $\tilde{\mathbf{H}}_{k,i} \triangleq \mathbf{H}_{\text{dir},k,i}^\top + \mathbf{H}_{\text{ref},k}^\top (\Phi - \mathbf{I}) \mathbf{H}_{\text{ref},i} \in \mathbb{C}^{N \times N}$  and  $\tilde{\mathbf{H}}_k = \mathbf{H}_{\text{ref},k}^\top (\Phi - \mathbf{I}) \mathbf{H}_{\text{ref},k} \in \mathbb{C}^{N \times N}$ . Here,  $\mathbf{H}_{\text{dir},k,i} \in \mathbb{C}^{N \times N}$  represents the direct channel between the  $k^{\text{th}}$  and  $i^{\text{th}}$  FD users, while  $\mathbf{H}_{\text{ref},k} \in \mathbb{C}^{M \times N}$  denotes the channel between the  $k^{\text{th}}$  FD user and the RIS.

### A. Structural Scattering

The terms  $-\mathbf{H}_{\text{ref},k}^\top \mathbf{H}_{\text{ref},i}$  and  $-\mathbf{H}_{\text{ref},k}^\top \mathbf{H}_{\text{ref},k}$  represent structural scattering, which is also termed as specular reflection caused by the RIS when it is inactive. It is worth noting that the commonly used model that ignores structural scattering can be derived from this model by omitting the  $-\mathbf{I}$  term immediately

following  $\Phi$  in all channel expressions. Although structural scattering is often neglected in most RIS studies, it is more physics-compliant and can significantly impact system performance [27], [30]–[32]. Specifically, the relationship between the impedance and scattering matrix is given by [33]

$$\mathbf{S}_{RI} = \frac{\mathbf{Z}_{RI}}{2Z_0}, \quad \mathbf{S}_{IT} = \frac{\mathbf{Z}_{IT}}{2Z_0}, \quad (1)$$

$$\mathbf{S}_{RT} = \frac{1}{2Z_0} \left( \mathbf{Z}_{RT} - \frac{\mathbf{Z}_{RI}\mathbf{Z}_{IT}}{2Z_0} \right). \quad (2)$$

The transmission impedance matrices from the transmitter to receiver, from the transmitter to RIS, and from the RIS to receiver are denoted by  $\mathbf{Z}_{RT} \in \mathbb{C}^{N \times N}$ ,  $\mathbf{Z}_{IT} \in \mathbb{C}^{M \times N}$ , and  $\mathbf{Z}_{RI} \in \mathbb{C}^{N \times M}$ , respectively.  $Z_0$  is the characteristic impedance used to compute the S-parameters, typically equal to  $Z_0 = 50\Omega$ . Similarly,  $\mathbf{S}_{RT} \in \mathbb{C}^{N \times N}$ ,  $\mathbf{S}_{IT} \in \mathbb{C}^{M \times N}$ , and  $\mathbf{S}_{RI} \in \mathbb{C}^{N \times M}$ , denote the transmission scattering matrices from the transmitter to receiver, from the transmitter to RIS, and from the RIS to receiver, respectively.

In most existing RIS literature, scattering matrices between devices are regarded as wireless channels such that the following relationship is commonly used:

$$\mathbf{H}_{RT} = \mathbf{S}_{RT}, \quad \mathbf{H}_{RI} = \mathbf{S}_{RI}, \quad \mathbf{H}_{IT} = \mathbf{S}_{IT}. \quad (3)$$

In addition, the approximation of (2) that  $\mathbf{S}_{RT} \approx \frac{\mathbf{Z}_{RT}}{2Z_0}$  is assumed, thus the channel model can be expressed as

$$\mathbf{H} = \mathbf{H}_{RT} + \mathbf{H}_{RI}\Theta\mathbf{H}_{IT}. \quad (4)$$

However, the direct mapping from the scattering parameter to wireless channels is not always physically compliant. In contrast, since the impedance parameters  $\mathbf{Z}_{RT}$ ,  $\mathbf{Z}_{RI}$ , and  $\mathbf{Z}_{IT}$  capture the open-circuit radiation patterns between devices, they accurately characterize the wireless channels. With (2), the channel model is more accurately expressed as

$$\mathbf{H} = \mathbf{H}_{RT} + \mathbf{H}_{RI}(\Theta - \mathbf{I})\mathbf{H}_{IT}. \quad (5)$$

Comparing (4) and (5), we observe an additional term  $-\mathbf{H}_{RI}\mathbf{I}\mathbf{H}_{IT}$ , which refers to the structural scattering at RIS. In this sense, if we consider a completely obstructed direct channel, *i.e.*,  $\mathbf{Z}_{RT} = \mathbf{0}$ , and turn the RIS OFF, *i.e.*,  $\Theta = \mathbf{0}$ , then we have  $\mathbf{H} = -\mathbf{H}_{RI}\mathbf{H}_{IT}$  instead of being zero. This term exists since  $\Theta = \mathbf{0}$  is achieved by  $\mathbf{Z}_I = Z_0\mathbf{I}$  with  $\mathbf{Z}_I \in \mathbb{C}^{M \times M}$  denoting the impedance matrix of the  $M$ -port reconfigurable impedance network. This means that RIS still radiates due to the non-zero current in RIS elements. We incorporate structural scattering in our model to better understand its impact and highlight the performance advantages of NR-BD-RIS.

### B. Signal Model

With such accurate model, the received signal at the  $k^{\text{th}}$  FD user is given by

$$\begin{aligned} y_k = & \mathbf{w}_k^H \widetilde{\mathbf{H}}_{k,k-1} \mathbf{p}_k s_k + \underbrace{\mathbf{w}_k^H \mathbf{H}_{\text{SI},k} \mathbf{p}_{k+1} s_{k+1}}_{\text{Self-interference}} \\ & + \underbrace{\mathbf{w}_k^H \overline{\mathbf{H}}_k \mathbf{p}_{k+1} s_{k+1}}_{\text{Loop Interference}} + \underbrace{\sum_{i \in \mathcal{K}, i \neq k, k+1} \mathbf{w}_k^H \widetilde{\mathbf{H}}_{k,i-1} \mathbf{p}_i s_i}_{\text{MU Interference}} \quad (6) \\ & + \mathbf{w}_k^H \mathbf{n}_k, \forall k \in \mathcal{K}, \end{aligned}$$

where  $\mathbf{H}_{\text{SI},k} \in \mathbb{C}^{N \times N}$  represents the self-interference (SI) channel of the  $k^{\text{th}}$  FD user. Specifically,  $\mathbf{H}_{\text{SI},k} = \mathbf{H}_{\text{dir},k,k}$ . The additive Gaussian white noise (AWGN) is represented by  $\mathbf{n}_k \sim \mathcal{CN}(\mathbf{0}, \sigma^2 \mathbf{I}_N)$ . To prevent eavesdropping, we aim to suppress the signals from other users except  $(k-1)^{\text{th}}$  user, which are referred to as MU interference.

The signal-to-interference-plus-noise ratio (SINR) at the  $k^{\text{th}}$  FD user is calculated as

$$\gamma_k = \frac{|\mathbf{w}_k^H \widetilde{\mathbf{H}}_{k,k-1} \mathbf{p}_k|^2}{I_k(\mathbf{w}_k, \{\mathbf{p}_i\}_{i \neq k, k+1}, \Phi) + \|\mathbf{w}_k\|_F^2 \sigma^2}, \quad (7)$$

where the interference power term incorporating SI, loop interference, and MU interference is expressed by

$$\begin{aligned} I_k(\mathbf{w}_k, \{\mathbf{p}_i\}_{i \neq k, k+1}, \Phi) = & \sum_{i \in \mathcal{K}, i \neq k, k+1} |\mathbf{w}_k^H \widetilde{\mathbf{H}}_{k,i-1} \mathbf{p}_i|^2 \\ & + |\mathbf{w}_k^H \mathbf{H}_{\text{SI},k} \mathbf{p}_{k+1} + \mathbf{w}_k^H \overline{\mathbf{H}}_k \mathbf{p}_{k+1}|^2. \end{aligned} \quad (8)$$

### III. PROBLEM FORMULATION AND TRANSFORMATION

In this section, we formulate the weighted all-user sum-rate maximization problem for the secure FD wireless circulator. The optimization problem is then transformed using the fractional programming method into a more tractable form. In the optimization, we design the precoders and combiners of FD users, and the scattering matrix of the BD-RIS.

#### A. Problem Formulation

We aim to maximize the weighted sum-rate of all FD users:

$$f_o(\mathbf{P}, \mathbf{W}, \Phi) \triangleq \sum_{k \in \mathcal{K}} \alpha_k \log_2(1 + \gamma_k). \quad (9)$$

In (9),  $\alpha_k$  denotes the weight for each FD user, where the condition  $\sum_{k \in \mathcal{K}} \alpha_k = 1$  should be satisfied. Subsequently, the optimization problem is given by

$$\mathcal{P}1: \max_{\mathbf{P}, \mathbf{W}, \Phi} f_o(\mathbf{P}, \mathbf{W}, \Phi) \quad (10a)$$

$$\text{s.t.} \quad \|\mathbf{p}_k\|_F^2 \leq P_{k-1}, \quad \forall k \in \mathcal{K} \quad (10b)$$

$$\|\mathbf{w}_k\|_F^2 = 1, \quad \forall k \in \mathcal{K}, \quad (10c)$$

$$\Phi \in \mathcal{R}_i, i \in \{1, 2\}, \text{ select one for } i, \quad (10d)$$

$$\Phi \in \mathcal{S}_\ell, \ell \in \{1, 2, 3\}, \text{ select one for } \ell. \quad (10e)$$

The transmit and receive power constraints are represented by (10b) and (10c), respectively. The transmit power of the  $(k-1)^{\text{th}}$  FD user for sending signals to the  $k^{\text{th}}$  FD user is denoted by  $P_{k-1}$ . Constraint (10d) specifies the symmetry of the scattering matrix: for R-BD-RIS,  $\Phi \in \mathcal{R}_1 = \{\Phi | \Phi = \Phi^T\}$ , and for NR-BD-RIS,  $\Phi \in \mathcal{R}_2 = \{\Phi | \Phi \neq \Phi^T\}$ . Constraint (10e) enforces losslessness in the multi-port impedance network [10], [12], constraining  $\Phi$  as follows: *i*)  $\mathcal{S}_1 = \{\Phi = \text{diag}(\phi_1, \dots, \phi_M) | |\phi_m| = 1, \forall m \in \mathcal{M}\}$  for D-RIS, *ii*)  $\mathcal{S}_2 = \{\Phi = \text{blkdiag}(\Phi_1, \dots, \Phi_G) | \Phi_g^H \Phi_g = \mathbf{I}, \forall g \in \mathcal{G}\}$  for group-connected BD-RIS, and *iii*)  $\mathcal{S}_3 = \{\Phi | \Phi^H \Phi = \mathbf{I}\}$  for fully-connected BD-RIS. We adopt a fractional programming-based approach [34] to reformulate the problem into a more tractable form.

## B. Problem Transformation

**Lagrange Dual Transformation.** To address the complexity of the fractional term, we decouple it from the  $\log(\cdot)$  in the objective function (10a) using the Lagrangian dual transformation [34]. Thus, we have a more manageable summation involving a new fractional term, expressed as

$$f_l(\mathbf{P}, \mathbf{W}, \Phi) = \sum_{k \in \mathcal{K}} \alpha_k \left( \log_2(1 + \iota_k) - \iota_k + \frac{(1 + \iota_k) |\mathbf{w}_k^H \widetilde{\mathbf{H}}_{k,k-1} \mathbf{p}_k|^2}{\Gamma_k + \|\mathbf{w}_k\|_F^2 \sigma_k^2} \right), \quad (11)$$

where  $\boldsymbol{\iota} \triangleq [\iota_1, \dots, \iota_K]^\top \in \mathbb{R}^K$  is the auxiliary vector.  $\Gamma_k$  is defined by

$$\Gamma_k = I_k(\mathbf{w}_k, \{\mathbf{p}_i\}_{i \neq k, k+1}, \Phi) + |\mathbf{w}_k^H \widetilde{\mathbf{H}}_{k,k-1} \mathbf{p}_k|^2. \quad (12)$$

**Quadratic Transformation.** To further simplify the fractional term, we apply the quadratic transformation [34], converting the components into integral expressions. The retransformed objective function is given by

$$f_\tau(\mathbf{P}, \mathbf{W}, \Phi, \boldsymbol{\iota}, \boldsymbol{\tau}) = \sum_{k \in \mathcal{K}} \alpha_k \left( \log_2(1 + \iota_k) - \iota_k + 2\sqrt{1 + \iota_k} \operatorname{Re} \left\{ \tau_k^* \mathbf{w}_k^H \widetilde{\mathbf{H}}_{k,k-1} \mathbf{p}_k \right\} - |\tau_k|^2 (\Gamma_k + \|\mathbf{w}_k\|_F^2 \sigma_k^2) \right), \quad (13)$$

where  $\boldsymbol{\tau} \triangleq [\tau_1, \dots, \tau_K]^\top \in \mathbb{R}^K$  is another introduced auxiliary vector, leading to the reformulated optimization problem

$$\begin{aligned} \mathcal{P}2: \quad & \max_{\Phi, \mathbf{P}, \mathbf{W}, \boldsymbol{\iota}, \boldsymbol{\tau}} f_\tau(\mathbf{P}, \mathbf{W}, \Phi, \boldsymbol{\iota}, \boldsymbol{\tau}) \\ \text{s.t.} \quad & (10b), (10c), (10d), (10e). \end{aligned} \quad (14a)$$

## IV. SOLUTION TO ALL USER SUM-RATES MAXIMIZATION

The reformulated problem  $\mathcal{P}2$  is a multi-variable optimization problem with non-convex constraints. To solve it, we employ the block coordinate descent (BCD) method [35]. In this framework, all variables are fixed except for the optimized variable in one iteration. This process is repeated until convergence. Regarding the constraints, there are three main difficulties: *i*) constraints (10d) and (10e) are coupled, *ii*) the symmetry constraint (10d), and *iii*) the unitary constraint (10e) complicates the problem. Therefore, to decouple (10d) and (10e), we adopt the PDD method, which introduces a copy of the scattering matrix and penalty terms [36]. To handle the symmetry constraint (10d), linearization is applied to the scattering matrix to ensure that only the required elements are optimized. With the first two difficulties addressed, the sub-problem with the unitary constraint (10e) becomes an orthogonal Procrustes problem. This problem can be solved using the singular value decomposition (SVD) method and has a closed-form solution. The proposed design algorithm is summarized in Algorithm 1. The details of the sub-problems are presented in the following subsections. Additionally, the optimal solutions for each block are derived. The optimal solution of auxiliary vectors  $\boldsymbol{\iota}$  is derived in [34], i.e.,  $\iota_k^{\text{opt}} = \gamma_k$ .

---

### Algorithm 1: Proposed Algorithm for All User Sum-rate Design

---

**Input:**  $\mathbf{H}_{\text{Sl}}, \mathbf{H}_k, k \in \mathcal{K}$ .

**Output:**  $\Phi^{\text{opt}}, \mathbf{P}^{\text{opt}}, \mathbf{W}^{\text{opt}}$ .

---

- 1 Initialize  $\Phi, \mathbf{P}, \mathbf{W}, t = 1$ .
  - 2 **while** no convergence of objective function (14a) &  
 $t < t_{\max}$  **do**
    - 3 Update  $\iota_k^{\text{opt}}, k \in \mathcal{K}$  by (7).
    - 4 Update  $\tau_k^{\text{opt}}, k \in \mathcal{K}$  by (15).
    - 5 Update  $\mathbf{P}^{\text{opt}}$  by (20).
    - 6 Update  $\mathbf{W}^{\text{opt}}$  by (25).
    - 7 Update  $\Phi^{\text{opt}}$  by Algorithm 2.
    - 8  $t = t + 1$ .
  - 9 **end**
  - 10 Return  $\Phi^{\text{opt}}, \mathbf{P}^{\text{opt}}, \mathbf{W}^{\text{opt}}$ .
- 

**Auxiliary Vectors: Block  $\boldsymbol{\tau}$ .** The sub-problem is an unconstrained convex optimization when  $\mathbf{P}, \mathbf{W}, \Phi, \boldsymbol{\iota}$  are fixed. Consequently, the optimal  $\boldsymbol{\tau}^{\text{opt}}$  is obtained by setting  $\frac{\partial f_\tau(\mathbf{P}, \mathbf{W}, \Phi, \boldsymbol{\iota}, \boldsymbol{\tau})}{\partial \boldsymbol{\tau}} = \mathbf{0}$ , which yields

$$\tau_k^{\text{opt}} = \frac{\sqrt{1 + \iota_k} \mathbf{w}_k^H \widetilde{\mathbf{H}}_{k,k-1} \mathbf{p}_k}{\Gamma_k + \|\mathbf{w}_k\|_F^2 \sigma_k^2}. \quad (15)$$

**Transmit Precoder: Block  $\mathbf{P}$ .** Given that  $\mathbf{W}, \Phi, \boldsymbol{\iota}$ , and  $\boldsymbol{\tau}$  are fixed, we isolate the terms associated with  $\mathbf{P}$  given by

$$\begin{aligned} f_\tau(\mathbf{P}) = \sum_{k \in \mathcal{K}} \alpha_k \left( 2\sqrt{1 + \iota_k} \operatorname{Re} \left\{ \tau_k^* \mathbf{w}_k^H \widetilde{\mathbf{H}}_{k,k-1} \mathbf{p}_k \right\} - |\tau_k|^2 \left( |\mathbf{w}_k^H \mathbf{H}_{\text{Sl},k} \mathbf{p}_{k+1} + \mathbf{w}_k^H \widetilde{\mathbf{H}}_{k,k-1} \mathbf{p}_{k+1}|^2 \right. \right. \\ \left. \left. + \sum_{i \in \mathcal{K}, i \neq k+1} \mathbf{p}_i^H \widetilde{\mathbf{H}}_{k,i-1}^H \mathbf{w}_k \mathbf{w}_k^H \widetilde{\mathbf{H}}_{k,i-1} \mathbf{p}_i \right) \right). \end{aligned} \quad (16)$$

Thus, the optimization problem w.r.t  $\mathbf{P}$  is expressed as follows:

$$\mathcal{P}3: \max_{\mathbf{P}} f_\tau(\mathbf{P}) \quad (17a)$$

$$\text{s.t.} \quad \|\mathbf{p}_k\|_F^2 \leq P_{k-1}, \quad \forall k \in \mathcal{K}. \quad (17b)$$

Since both the objective function (17a) and the constraint (17b) are convex, the constraint can be incorporated into the objective function using the Lagrange multiplier method, based on the Karush–Kuhn–Tucker (KKT) conditions, by introducing a multiplier  $\mu$ . The components w.r.t  $\mathbf{p}_k$  are

$$\begin{aligned} f_\tau(\mathbf{p}_k) = \alpha_k \left( 2\sqrt{1 + \iota_k} \operatorname{Re} \left\{ \tau_k^* \mathbf{w}_k^H \widetilde{\mathbf{H}}_{k,k-1} \mathbf{p}_k \right\} - |\tau_k|^2 \left( \mathbf{p}_k^H \widetilde{\mathbf{H}}_{k,k-1}^H \sum_{p \in \mathcal{K}} \mathbf{w}_p \mathbf{w}_p^H \widetilde{\mathbf{H}}_{k,k-1} \mathbf{p}_k \right) \right. \\ \left. - \alpha_{k-1} |\tau_{k-1}|^2 |\mathbf{w}_{k-1}^H \mathbf{H}_{\text{Sl},k-1} \mathbf{p}_k + \mathbf{w}_{k-1}^H \widetilde{\mathbf{H}}_{k-1} \mathbf{p}_k|^2 \right). \end{aligned} \quad (18)$$

The unconstrained sub-problem is given below

$$\mathcal{P}4: \max_{\mathbf{p}_k} f_\tau(\mathbf{p}_k) - \mu (\|\mathbf{p}_k\|_F^2 - P_{k-1}). \quad (19a)$$

The optimal solution for each precoder  $\mathbf{p}_k$  can be derived using the first-order optimality condition:

$$\mathbf{p}_k^{\text{opt}} = (\alpha_k |\tau_k|^2 \boldsymbol{\zeta}_{1,k} + \alpha_{k-1} |\tau_{k-1}|^2 \boldsymbol{\zeta}_{2,k} + \mu^{\text{opt}} \mathbf{I})^{-1} \alpha_k \sqrt{1 + \iota_k} \tau_k \widetilde{\mathbf{H}}_{k,k-1}^H \mathbf{w}_k, \quad (20)$$

where  $\zeta_{1,k}$  and  $\zeta_{2,k}$  are defined by

$$\zeta_{1,k} = \widetilde{\mathbf{H}}_{k,k-1}^H \sum_{p \in \mathcal{K}} \mathbf{w}_p \mathbf{w}_p^H \widetilde{\mathbf{H}}_{k,k-1}, \quad (21)$$

$$\begin{aligned} \zeta_{2,k} = & (\mathbf{H}_{\text{SI},k-1}^H \mathbf{w}_{k-1} \mathbf{w}_{k-1}^H \mathbf{H}_{\text{SI},k-1} + \overline{\mathbf{H}}_{k-1}^H \mathbf{w}_{k-1} \mathbf{w}_{k-1}^H \overline{\mathbf{H}}_{k-1}) \\ & + 2 \text{Re} \left\{ \mathbf{H}_{\text{SI},k-1}^H \mathbf{w}_{k-1} \mathbf{w}_{k-1}^H \overline{\mathbf{H}}_{k-1}^H \right\}, \end{aligned} \quad (22)$$

and we can use bisection search to find  $\mu^{\text{opt}}$ .

**Receive Combiner: Block  $\mathbf{W}$ .** Given fixed values for  $\mathbf{P}, \Phi, \iota$ , and  $\tau$ , the objective function w.r.t  $\mathbf{W}$  is expressed as

$$\begin{aligned} f_\tau(\mathbf{W}) = & \sum_{k \in \mathcal{K}} \alpha_k \left( 2\sqrt{1 + \iota_k} \text{Re} \left\{ \tau_k^* \mathbf{w}_k^H \widetilde{\mathbf{H}}_{k,k-1} \mathbf{p}_k \right\} \right. \\ & - |\tau_k|^2 \left( \left| \mathbf{w}_k^H \mathbf{H}_{\text{SI},k} \mathbf{p}_{k+1} + \mathbf{w}_k^H \overline{\mathbf{H}}_k \mathbf{p}_{k+1} \right|^2 \right. \\ & \left. \left. + \mathbf{w}_k^H \left( \sum_{i \in \mathcal{K}, i \neq k+1} \widetilde{\mathbf{H}}_{k,i-1} \mathbf{p}_i \mathbf{p}_i^H \widetilde{\mathbf{H}}_{k,i-1}^H \right) \mathbf{w}_k + \|\mathbf{w}_k\|_F^2 \sigma^2 \right) \right). \end{aligned} \quad (23)$$

Therefore, the sub-optimization problem with regard to  $\mathbf{W}$  is

$$\mathcal{P5}: \max_{\mathbf{W}} f_\tau(\mathbf{W}) \quad (24a)$$

$$\text{s.t.} \quad \|\mathbf{w}_k\|_F^2 = 1, \quad \forall k \in \mathcal{K}. \quad (24b)$$

The constraint (24b) is non-convex, making the problem hard to tackle with. Therefore, we relax this constraint and the sub-problem becomes unconstrained. Finally, the solution is normalized to satisfy normalization constraint. Specifically, We still take the derivative of the objective function w.r.t  $\mathbf{w}_k$  and set it to zero, leading to the optimal solution for each combiner  $\mathbf{w}_k$ . The expression of the optimal combiner  $\mathbf{w}_k^{\text{opt}}$  is given by

$$\mathbf{w}_k^{\text{opt}} = (|\tau_k|^2 \xi_k)^{-1} (\sqrt{1 + \iota_k} \tau_k^* \widetilde{\mathbf{H}}_{k,k-1} \mathbf{p}_k), \quad (25)$$

where  $\xi$  is given by

$$\begin{aligned} \xi_k = & (\mathbf{H}_{\text{SI},k} \mathbf{p}_{k+1} \mathbf{p}_{k+1}^H \mathbf{H}_{\text{SI},k}^H + 2 \text{Re} \{ \overline{\mathbf{H}}_k \mathbf{p}_{k+1} \mathbf{p}_{k+1}^H \mathbf{H}_{\text{SI},k}^H \} \\ & + \overline{\mathbf{H}}_k \mathbf{p}_{k+1} \mathbf{p}_{k+1}^H \overline{\mathbf{H}}_k^H) + \sum_{i \in \mathcal{K}, i \neq k+1} \widetilde{\mathbf{H}}_{k,i-1} \mathbf{p}_i \mathbf{p}_i^H \widetilde{\mathbf{H}}_{k,i-1}^H + \sigma^2. \end{aligned} \quad (26)$$

Finally, we normalize the obtained solution  $\mathbf{w}_k^{\text{opt}}$  to satisfy the constraint (24b).

**BD-RIS Scattering Matrix:  $\Phi$ .** Given fixed values for  $\mathbf{P}, \mathbf{W}, \iota, \tau$ , we isolate the terms related to  $\Phi$ , expressed as

$$\begin{aligned} f_\tau(\Phi) = & \sum_{k \in \mathcal{K}} \alpha_k \left( 2\sqrt{1 + \iota_k} \text{Re} \left\{ \tau_k^* \mathbf{w}_k^H \widetilde{\mathbf{H}}_{k,k-1} \mathbf{p}_k \right\} \right. \\ & - |\tau_k|^2 \left( \left| \mathbf{w}_k^H \mathbf{H}_{\text{SI},k} \mathbf{p}_{k+1} + \mathbf{w}_k^H \overline{\mathbf{H}}_k \mathbf{p}_{k+1} \right|^2 \right. \\ & \left. \left. + \sum_{i \in \mathcal{K}, i \neq k+1} \left| \mathbf{w}_k^H \widetilde{\mathbf{H}}_{k,i-1} \mathbf{p}_i \right|^2 \right) \right) \\ = & 2 \text{Re} \{ \text{Tr}(\mathbf{C}_1 \Phi) \} - 2 \text{Re} \{ \text{Tr}(\mathbf{C}_2 \Phi) \} - \text{Tr}(\mathbf{A} \Phi \mathbf{B} \Phi^H) \\ & + 2 \text{Re} \{ \text{Tr}(\mathbf{C}_3 \Phi) \} - 2 \text{Re} \{ \text{Tr}(\mathbf{C}_4 \Phi) \} + 2 \text{Re} \{ \text{Tr}(\mathbf{C}_5 \Phi) \}. \end{aligned} \quad (27)$$

Table I provides the definitions of the newly introduced notations. Since the single- and fully-connected BD-RIS are special

**Algorithm 2:** Algorithm for Optimizing BD-RIS Scattering Matrix  $\Phi$

**Input:**  $\mathbf{P}, \mathbf{W}, \iota_k, \tau_k, \mathbf{H}_{\text{SI}}, \mathbf{H}_k, k \in \mathcal{K}$ .

**Output:**  $\Phi^{\text{opt}}$ .

```

1 Initialize  $\{\Phi_g\}, \{\Psi_g\}, \{\Lambda_g\}, \rho, t_{\text{inner}} = t_{\text{outer}} = 1$ .
2 for  $g \leftarrow 1$  to  $G$  do
3   while  $\|\Phi_g - \Psi_g\|_\infty > \varepsilon$  &  $t_{\text{outer}} < t_{\text{outer max}}$  do
4     while no convergence of objective function
       (31a) &  $t_{\text{inner}} < t_{\text{inner max}}$  do
5       Update  $\Phi_g$  by (39).
6       Update  $\Psi_g$  by (41).
7        $t_{\text{inner}} = t_{\text{inner}} + 1$ .
8     end
9     if  $\|\Phi_g - \Psi_g\|_\infty < \epsilon$  then
10       $\Lambda_g = \Lambda_g + \rho^{-1}(\Phi_g - \Psi_g)$ .
11    else
12       $\rho = c\rho$ .
13    end
14     $t_{\text{outer}} = t_{\text{outer}} + 1$ .
15  end
16 end
17 return  $\Phi^{\text{opt}} = \text{blkdiag}(\Phi_1^{\text{opt}}, \dots, \Phi_G^{\text{opt}})$ .
```

TABLE I  
NEWLY INTRODUCED NOTATIONS

$\mathbf{A} = \sum_{k \in \mathcal{K}} \alpha_k  \tau_k ^2 \mathbf{H}_{\text{ref},k}^* \mathbf{w}_k \mathbf{w}_k^H \mathbf{H}_{\text{ref},k}^\top$	$\mathbf{B} = \sum_{i \in \mathcal{K}} \mathbf{H}_{\text{ref},i-1} \mathbf{p}_i \mathbf{p}_i^H \mathbf{H}_{\text{ref},i-1}^H$
$\mathbf{C}_1 = \sum_{k \in \mathcal{K}} \alpha_k \sqrt{1 + \iota_k} \tau_k^* \mathbf{H}_{\text{ref},k} \mathbf{p}_{k+1} \mathbf{p}_{k+1}^H \mathbf{H}_{\text{ref},k}^\top$	$\mathbf{C}_3 = \mathbf{A} \mathbf{B}$
$\mathbf{C}_2 = \sum_{k \in \mathcal{K}} \alpha_k  \tau_k ^2 \mathbf{H}_{\text{ref},k} \mathbf{p}_{k+1} \mathbf{p}_{k+1}^H \mathbf{H}_{\text{SI},k}^H \mathbf{w}_k \mathbf{w}_k^H \mathbf{H}_{\text{ref},k}^\top$	
$\mathbf{C}_4 = \sum_{k \in \mathcal{K}} \alpha_k  \tau_k ^2 \sum_{i \in \mathcal{K}} \mathbf{H}_{\text{ref},i-1} \mathbf{p}_i \mathbf{p}_i^H \mathbf{H}_{\text{dir},k,i-1}^H \mathbf{w}_k \mathbf{w}_k^H \mathbf{H}_{\text{ref},k}^\top$	
$\mathbf{C}_5 = \sum_{k \in \mathcal{K}} \alpha_k  \tau_k ^2 \mathbf{H}_{\text{ref},k} \mathbf{p}_{k+1} \mathbf{p}_{k+1}^H \mathbf{H}_{\text{dir},k,k}^H \mathbf{w}_k \mathbf{w}_k^H \mathbf{H}_{\text{ref},k}^\top$	

cases of the group-connected case, the following sub-problem w.r.t. the group-connected BD-RIS is used for explanation:

$$\mathcal{P6}: \max_{\Phi} f_\tau(\Phi) \quad (28a)$$

$$\text{s.t.} \quad \Phi \in \mathcal{R}_i, i \in \{1, 2\}, \text{ select one value for } i, \quad (28b)$$

$$\Phi \in \mathcal{S}_2. \quad (28c)$$

The main challenges in solving the sub-problem  $\mathcal{P6}$  are the unitary constraint (28c) and the symmetry constraint (28b). Below, we present a general approach for designing the scattering matrix  $\Phi$  applicable to both NR-BD-RIS and R-BD-RIS.

#### A. PDD Method to Decouple (28c) and (28b)

In this section, we employ the PDD method [36], [37] to decouple constraints (28c) and (28b). The PDD framework is a two-loop iterative approach [36], comprising an inner loop and an outer loop. The inner loop addresses the augmented Lagrangian problem using BCD approach, and the outer loop adjusts the Lagrangian dual variables  $\{\Lambda_g\}$  and the penalty coefficient  $\rho$  until convergence (i.e.,  $\|\Phi - \Psi\|_\infty \leq \varepsilon$ ). Specifically, in the inner loop, each  $\Phi_g, \forall g \in \mathcal{G}$ , is optimized iteratively. The outer loop adjusts  $\{\Lambda_g\}$  and  $\rho$  to ensure the



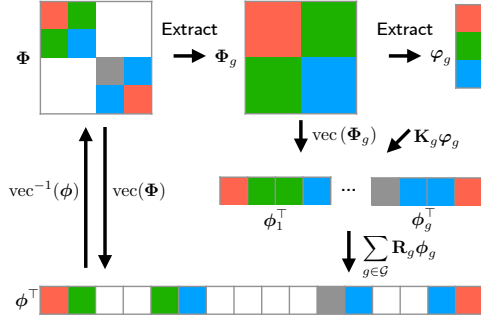


Fig. 5. The linear reformulation and reconstruction for the reciprocal case.

algorithm converges. This algorithm is concluded in Algorithm 2. To decouple constraints (28c) and (28b), we introduce a copy  $\{\Psi_g\}$  of  $\{\Phi_g\}$  and enforce the equality constraint  $\Psi_g = \Phi_g, \forall g \in \mathcal{G}$ . We then have the following problem:

$$\mathcal{P7} : \max_{\Phi, \Psi} f_\tau(\Phi) \quad (29a)$$

$$\text{s.t.} \quad \Psi_g^H \Psi_g = \mathbf{I}, \quad \forall g \in \mathcal{G}, \quad (29b)$$

$$\Phi_g = \Psi_g, \quad \forall g \in \mathcal{G}, \quad (29c)$$

$$(28b).$$

Subsequently, we reformulate the problem by introducing a penalty term to enforce the equality constraint (29c) with the Lagrangian dual variable and penalty coefficient  $\Lambda_g \in \mathbb{C}^{M \times M}, \forall g \in \mathcal{G}$ , and  $1/\rho$ , respectively. This allows us to optimize  $\Phi_g$  and  $\Psi_g$  separately while ensuring they converge to the same solution. The reformulated problem is given by

$$L(\{\Phi_g\}, \{\Psi_g\}, \{\Lambda_g\}, \rho) = -f_\tau(\Phi) + \frac{1}{2\rho} \sum_{g \in \mathcal{G}} \|\Phi_g - \Psi_g\|^2 + \sum_{g \in \mathcal{G}} \text{Re}\{\text{Tr}(\Lambda_g^H (\Phi_g - \Psi_g))\}, \quad (30)$$

We then have the reformulated problem as

$$\mathcal{P8} : \min_{\Phi, \Psi} L(\{\Phi_g\}, \{\Psi_g\}, \{\Lambda_g\}, \rho) \quad (31a)$$

$$\text{s.t.} \quad (28b), (29b).$$

The inner and outer loop update processes are provided below.

### B. Inner Loop

In the inner loop, we first preprocess the scattering matrix  $\Phi_g$  to a linear formulation, which is explained in Fig. 5. Subsequently, we update  $\Phi_g$  and  $\Psi_g$ .

1) *Linear Reformulation of Symmetry Constraint*: We utilize the linear reformulation to tackle the symmetry constraint (29b). We extract the necessary elements of the scattering matrix  $\Phi_g$  and store them in a vector  $\varphi_g$ . For NR-BD-RIS, all elements of  $\Phi_g$  are extracted, while for R-BD-RIS, only the diagonal and lower-triangular elements are extracted. The vector  $\varphi_g$  is constructed in a column-wise order. The reconstruction of the full vector  $\phi_g = \text{vec}(\Phi_g)$  from  $\varphi_g$  is

achieved using a permutation matrix  $\mathbf{K}_g$  defined in [28], which depends on whether it is NR-BD-RIS or R-BD-RIS.

$$\phi_g \triangleq \text{vec}(\Phi_g) = \mathbf{K}_g \varphi_g, \quad \forall g \in \mathcal{G}. \quad (32)$$

To position the group vector  $\phi_g$  into the overall vector  $\phi$ , a reshaping matrix  $\mathbf{R}_g \in \mathbb{B}^{M^2 \times M_g^2}$  is required and defined in [28]. The whole mapping process is illustrated in Fig. 5 and the mathematical formulation is given by

$$\phi \triangleq \text{vec}(\Phi) = \sum_{g \in \mathcal{G}} \mathbf{R}_g \phi_g, \quad (33)$$

After the symmetry constraint is reformulated, we can apply the PDD method to optimize the scattering matrix  $\Phi$ .

2)  $\Phi_g$  in the inner loop: With following transformations with trace operation

$$\text{Tr}(\mathbf{C}\Phi) = \text{vec}^\top(\mathbf{C}^\top) \phi = \sum_{g \in \mathcal{G}} \text{vec}^\top(\mathbf{C}^\top) \mathbf{R}_g \mathbf{K}_g \varphi_g, \quad (34)$$

$$\begin{aligned} \text{Tr}(\mathbf{B}\Phi\mathbf{A}\Phi^H) &= \phi^H (\mathbf{A}^\top \otimes \mathbf{B}) \phi \\ &= \left( \sum_{g \in \mathcal{G}} \mathbf{R}_g \mathbf{K}_g \varphi_g \right)^H (\mathbf{A}^\top \otimes \mathbf{B}) \left( \sum_{g \in \mathcal{G}} \mathbf{R}_g \mathbf{K}_g \varphi_g \right), \end{aligned} \quad (35)$$

the sub-problem w.r.t  $\varphi_g$  is formulated as

$$\mathcal{P9} : \min_{\varphi_g} L(\varphi_g) = \varphi_g^H \Delta \varphi_g - 2 \text{Re}\{\varphi_g^H \delta\}. \quad (36a)$$

The vectorization is defined as  $\psi_g \triangleq \text{vec}(\Psi_g)$ ,  $\lambda_g \triangleq \text{vec}(\Lambda_g)$ ,

$$\Delta = \mathbf{K}_g^H \mathbf{R}_g^H (\mathbf{A}^\top \otimes \mathbf{B}) \mathbf{R}_g \mathbf{K}_g + \frac{1}{2\rho} \mathbf{K}_g^H \mathbf{K}_g, \quad (37)$$

$$\begin{aligned} \delta &= \mathbf{K}_g^H \mathbf{R}_g^H \left( \text{vec}^*(\mathbf{C}_1^\top) - \text{vec}^*(\mathbf{C}_2^\top) + \text{vec}^*(\mathbf{C}_3^\top) \right. \\ &\quad \left. - \text{vec}^*(\mathbf{C}_4^\top) + \text{vec}^*(\mathbf{C}_5^\top) \right) + \frac{1}{2\rho} \mathbf{K}_g^H \mathbf{K}_g \psi_g - \frac{1}{2} \mathbf{K}_g^H \lambda_g. \end{aligned} \quad (38)$$

$\mathcal{P9}$  is an unconstrained convex optimization problem, and the optimal solution can be obtained by solving  $\frac{\partial L(\varphi_g)}{\partial \varphi_g} = 0$ . The optimal solution is then given by

$$\varphi_g^{\text{opt}} = \Delta^{-1} \delta. \quad (39)$$

3)  $\Psi_g$  in the inner loop: We fix the other variables and optimize  $\Psi_g$  in the inner loop. The optimization problem is formulated as follows:

$$\mathcal{P10} : \min_{\Psi_g} \|\Psi_g - (\rho \Lambda_g + \Phi_g)\|_F^2, \quad (40a)$$

$$\text{s.t.} \quad \Psi_g^H \Psi_g = \mathbf{I}. \quad (40b)$$

This problem is called orthogonal procrustes problem and has a close-form solution [37]–[40]. The solution is given by

$$\Psi_g^{\text{opt}} = \mathbf{U}_g \mathbf{V}_g^H. \quad (41)$$

Subsequently, we utilize singular vector decomposition (SVD) of  $\rho \Lambda_g + \Phi_g$  to obtain unitary matrices  $\mathbf{U}_g$ , and  $\mathbf{V}_g$ .

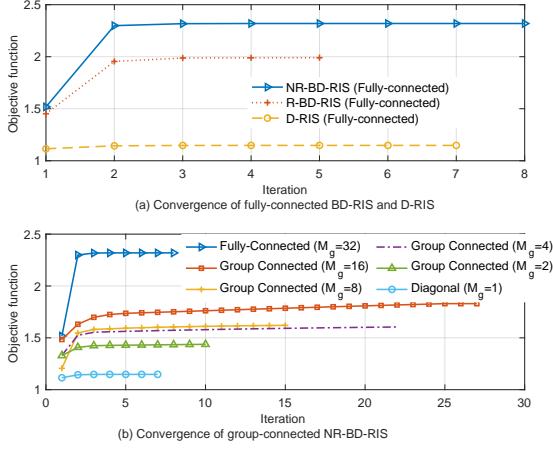


Fig. 6. Convergence analysis for Algorithm 1 with both direct and reflected links, using RIS elements  $M = 32$ . The 3 FD UEs are located at  $30^\circ$ ,  $90^\circ$ , and  $150^\circ$ , respectively. (a) Convergence for fully-connected NR-BD-RIS, R-BD-RIS, and D-RIS. (b) Convergence for group-connected NR-BD-RIS with varying group sizes.

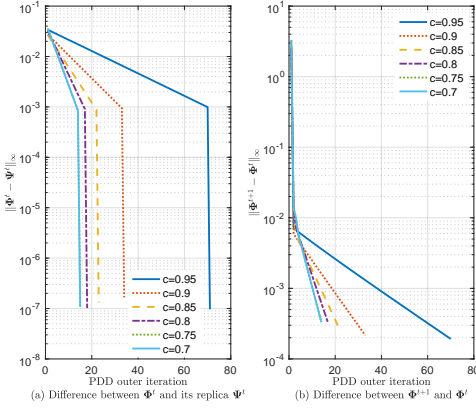


Fig. 7. Convergence analysis for Algorithm 2 (PDD) with both direct and reflected links for different  $c$  values, using  $M = 32$  and  $N = 1$ . The 3 FD UEs are located at  $30^\circ$ ,  $90^\circ$ , and  $150^\circ$ . (a) Convergence of the scattering matrix  $\Phi$  and its replica  $\Psi$ , measured by  $\|\Phi - \Psi\|_\infty$ . (b) Convergence of the scattering matrix  $\Phi$  between consecutive iterations, measured by  $\|\Phi - \Phi^{\text{prev}}\|_\infty$ .

### C. Outer loop

After the inner loop converges, the dual variable  $\Lambda_g$  and the penalty coefficient  $\rho$  are updated. The convergence condition is defined as  $\|\Phi_g - \Psi_g\|_\infty < \epsilon$ , where  $\epsilon$  is a small positive constant. If the convergence condition is satisfied, we update the dual variable as follows:

$$\Lambda_g = \Lambda_g + \rho^{-1}(\Phi_g - \Psi_g). \quad (42)$$

Otherwise, if the convergence condition is not satisfied, this means that the equality between  $\Phi_g$  and  $\Psi_g$  is not reached. We thus update the penalty coefficient  $\rho$  as  $\rho = c\rho$ , where  $c \in (0, 1)$  is the penalty scaling factor. Once the optimal  $\Phi_g^{\text{opt}}$  for each group is obtained, the overall scattering matrix  $\Phi^{\text{opt}}$  is reconstructed by combining the group matrices, i.e.,  $\Phi^{\text{opt}} = \text{blkdiag}(\Phi_1, \dots, \Phi_G)$ .

### D. Convergence Analysis

The convergence of the designed algorithms are analyzed and we show that the value of the objective function (31a) converges to at least a local optimal solution. Let  $v^t$  denote the objective function value (14a) at the  $t^{\text{th}}$  iteration. In Algorithm 1, each block optimization problem is solved iteratively. A special block involves the PDD method for updating the scattering matrix  $\Phi_g$  for each group  $g \in \mathcal{G}$ , as formulated in the sub-optimization  $\mathcal{P}8$ . In the inner loop of the PDD method, the sub-problem w.r.t.  $\Phi_g$ , i.e.,  $\mathcal{P}9$ , is convex and has a unique optimal solution. Similarly, the sub-problem w.r.t.  $\Psi_g$ , i.e.,  $\mathcal{P}10$ , is also convex and has a unique optimal solution. Consequently, the value of the objective function (31a) in  $\mathcal{P}8$  is monotonically non-increasing. Since the objective function (31a) is bounded below by zero, the inner loop is guaranteed to converge to a local optimal solution. The outer loop of the PDD method converges to a KKT point because the augmented Lagrangian progressively enforces constraint satisfaction while updating the dual variables [36]. Therefore, the solution for  $\Phi$  is guaranteed to be a local optimal solution. When the other variables are fixed, each block optimization problem for  $\iota$ ,  $\tau$ ,  $\mathbf{P}$ , and  $\Phi$  is convex and has a unique optimal solution. Consequently, the value of the objective function (14a) is monotonically non-decreasing after each iteration, i.e.,  $v^t \geq v^{t-1}$ . Since the objective function (14a) is bounded above, it converges to a local optimum.

We evaluate the convergence performance of the proposed Algorithm 1 and the PDD method in Algorithm 2 through simulations. We consider  $K = 3$  FD users, set the RIS element count to  $M = 32$ , and include direct links to demonstrate the general applicability. The convergence results are provided in Fig. 6 (a) for fully-connected NR-BD-RIS, R-BD-RIS, and D-RIS. It is observed that Algorithm 1 works for all 3 types of RIS, and converges within 10 iterations. The fully-connected NR-BD-RIS achieving the largest values. Additionally, Fig. 6 (b) presents the convergence performance for group-connected NR-BD-RIS. The values of objective function decrease as the group size  $M_g$  becomes smaller. The convergence of the PDD method, used to optimize  $\Phi$ , is also analyzed. In Fig. 7 (a), the difference between  $\Phi$  and its replica  $\Psi$  in the outer loop is shown. Convergence is achieved within 80 iterations, with the equality constraint (29c) being well satisfied, as indicated by  $\|\Phi - \Psi\|_\infty < 10^{-6}$ . Fig. 7 (b) presents the difference in  $\Phi$  between consecutive iterations, which decreases to approximately  $10^{-3}$ . To conclude, the PDD algorithm can converge faster if a smaller penalty parameter  $c$  is adopted. Additionally, an appropriate range for the penalty parameter is  $c \in (0.7, 0.95)$ .

### E. Complexity Analysis

Within the BCD framework, each block is updated iteratively. The computational complexity for updating  $\iota$  and  $\tau$  is  $\mathcal{O}(K^2 M^2)$  per iteration. Updating the precoder  $\mathbf{P}$  involves matrix inversion and bisection search, resulting in a complexity of  $\mathcal{O}(K(M^2 + I_b N^3))$ , where  $I_b$  denotes the number of bisection search iterations. Similarly, updating the combiner  $\mathbf{W}$  needs  $\mathcal{O}(KN^3)$  operations because of the matrix inversion.



PDD method to optimize the scattering matrix  $\Phi$  is the most computationally intensive step. Specifically, the computation of (39) involves the Kronecker product, contributing a complexity of  $\mathcal{O}(M_g^2 M^4)$ , while the SVD operation in (41) adds  $\mathcal{O}(M_g^3)$ . As a result, the computational complexity of Algorithm 2 is  $\mathcal{O}(GI_{\text{outer}}I_{\text{inner}}M_g^2M^4)$ , where  $I_{\text{outer}}$  is the outer iteration number, and  $I_{\text{inner}}$  is inner iteration number in the PDD method. Combining these results, the total computational complexity of the iterative optimization algorithm is  $\mathcal{O}(I_{\text{BCD}}GI_{\text{outer}}I_{\text{inner}}M_g^2M^4)$ , where  $I_{\text{BCD}}$  denotes BCD iteration number needed for convergence.

## V. NUMERICAL EVALUATION

We use numerical results to explain the one-way secure transmission and eavesdropping prevention in this FD wireless circulator systems. We also show the advantages of the NR-BD-RIS over the R-BD-RIS and D-RIS, considering both direct and reflected links. We investigate the impact of the number of RIS elements and the group size of the RIS on the sum-rate performance. Additionally, we compare the sum-rate performance of the NR-BD-RIS with the R-BD-RIS and D-RIS under varying relative locations of the FD users. To provide further insights, we illustrate the impinging and reflected beampatterns for the three types of RIS and discuss reasons behind the superior performance of the NR-BD-RIS and how eavesdropping is prevented. We also evaluate weighed sum-rate region by varying the weights  $\alpha_i, \forall i \in \mathcal{K}$ . The rate regions for the three users highlight the trade-offs in performance among them. Finally, we investigate the sum-rate performance of the NR-BD-RIS with varying numbers of TX and RX antennas at each FD user and the number of FD users.

The proposed algorithm is applicable to scenarios both with and without structural scattering. Note that the presented algorithm is designed for the case with structural scattering. In fact, the case without structural scattering is simpler in terms of optimization design. To evaluate the performance without structural scattering, the algorithm can be modified by removing the  $-\mathbf{I}$  term after  $\Phi$  in all channel expressions. In the simulations, direct links are considered in the sum-rate performance evaluation with respect to the number of RIS elements. These results confirm that the NR-BD-RIS provides performance gains over R-BD-RIS and D-RIS, even in the presence of direct links. In subsequent simulations, to better emphasize the benefits of the NR-BD-RIS, we assume that all direct links are blocked.

### A. Simulation Environment

The 2D coordinate system of the FD wireless circulator with RIS is shown in Fig. 8. Each FD user is equipped with  $N$  TX and  $N$  RX antennas. The channel models between the RIS and FD users include both large-scale and small-scale fading [2]. The large-scale fading is modeled using a distance-dependent path loss  $\text{PL}_i = \zeta_0 (d_i/d_0)^{-\varepsilon_i}, \forall i \in \mathcal{K}$ , where  $\zeta_0$  is the attenuation factor at a reference distance  $d_0 = 1$  m,  $d_i$  is the distance between the RIS and FD users, and  $\varepsilon_i$  is the path loss exponent for each user. The small-scale fading is modeled using Rician fading, where the Rician factor  $\kappa_i, \forall i \in$

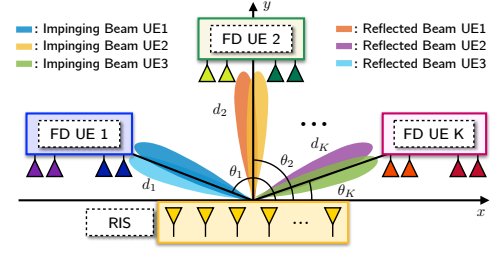


Fig. 8. 2D coordinate system for the FD wireless circulator system enabled by RIS. The optimal impinging and reflected beampatterns are depicted.

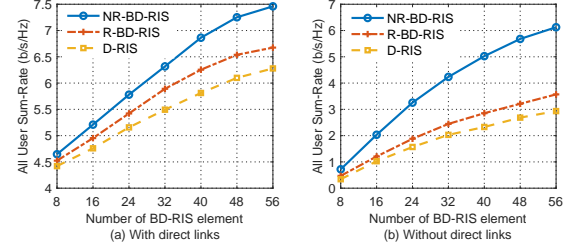


Fig. 9. Sum-rates versus the number of RIS element for the three RIS types: (a) with direct links and (b) without direct links. The NR-BD-RIS and R-BD-RIS are with fully-connected architecture. The 3 FD users are positioned at  $30^\circ$ ,  $90^\circ$ , and  $150^\circ$ . Structural scattering is included, and the numbers of Tx and Rx antennas are  $N = 1$ .

$\mathcal{K}$ , represents the power ratio between the line-of-sight (LoS) component and the non-LoS component.

We set  $\zeta_0 = -30$  dB, with a path loss exponent of  $\varepsilon_i = 2.2, \forall i \in \mathcal{K}$  for RIS-to-FD user channels. The direct links are assumed to be weak, with a path loss exponent of  $\varepsilon_i = 3.3$  [37]. The distances between the RIS and the FD users are set to  $d_1 = d_2 = d_3 = 35$  m. The Rician factor is set to  $\kappa_i = 5$  to account for the LoS component. The transmit power of each FD user is  $P_i = 20$  dBm,  $\forall i \in \mathcal{K}$ , and the noise power at the FD users is  $\sigma^2 = -80$  dBm. Since SI is not the primary focus of this study, it is assumed to be well mitigated to the noise level. This is achieved by using cancellation techniques in the propagation domain [41], the analog domain [42], and the digital domain [43]. The channel estimation is assumed to be perfect, and the CSI is available at each FD user through BD-RIS channel estimation techniques [29].

### B. Sum-rates over RIS elements

We analyze how number of RIS element affects the sum-rate performance. The 3 FD UEs are positioned at  $30^\circ$ ,  $90^\circ$ , and  $150^\circ$ , respectively, with each equipped with  $N = 1$  TX and RX antennas. Fig. 9 (a) and (b) illustrate the sum-rates versus the number of RIS element, considering scenarios with and without direct links, respectively. The results show that the NR-BD-RIS consistently outperforms the R-BD-RIS and D-RIS. When number of RIS element increases, the sum-rate performance of the NR-BD-RIS improves, and its advantage over the other two RIS types becomes more obvious. This is attributed to the NR-BD-RIS's ability to break channel reciprocity and support multiple directions for FD users. Comparing the scenarios with and without direct links, the NR-BD-RIS maintains its superior performance. However, the

performance gap between the NR-BD-RIS and the other two RIS types is smaller with direct links in Fig. 9 (a), compared to the case without direct links, as shown in Fig. 9 (b). This is because direct links provide additional communication paths for the FD users, reducing performance gain.

### C. Sum-rates

To highlight the advantages of the NR-BD-RIS, we assume that the direct links are blocked, and the FD users connect exclusively via the RIS. This section presents the all-user sum-rates to showcase the superior performance of the NR-BD-RIS compared to the R-BD-RIS and D-RIS in the wireless circulator scenario.

1) *Sum-rates versus One Moving FD UE*: We assign equal weights to the three FD UEs,  $\alpha_1 = \alpha_2 = \alpha_3 = 1/3$ , and set the number of RIS element to  $M = 16$ . Two scenarios are considered: in Case 1, FD UE 1 and FD UE 2 are fixed at  $30^\circ$  and  $90^\circ$ , respectively, while in Case 2, their locations are set to  $60^\circ$  and  $105^\circ$ . The location of FD UE 3 is then varied from  $0^\circ$  to  $180^\circ$  in increments of  $1^\circ$ .

In Fig. 10 (a), the NR-BD-RIS consistently outperforms the R-BD-RIS and D-RIS in most cases. Specifically, the NR-BD-RIS has the same level of sum-rate performance as the other two RIS types when FD UE 3 is aligned with either FD UE 1 ( $30^\circ$ ) or FD UE 2 ( $90^\circ$ ). This is because R-BD-RIS and D-RIS can support one impinging direction and one reflected direction. However, when FD UE 3 is not aligned with FD UE 1 or FD UE 2, the NR-BD-RIS demonstrates a clear advantage, as it can support multiple directions, resulting in a higher all-user sum-rate. In Fig. 10 (b), structural scattering is included, and the NR-BD-RIS still achieves the best sum-rate performance. Additionally, an enhancement is observed at the supplementary angle, *i.e.*,  $150^\circ$ , corresponding to FD UE 1's location ( $30^\circ$ ). This specular reflection condition can be explained as follows. Considering the received power at the  $k^{\text{th}}$  user, where the TX and RX antennas are set to  $N = 1$ , the received power is determined by the channel strength:  $\eta_k = |\mathbf{h}_k^\top (\mathbf{\Phi} - \mathbf{I}) \mathbf{h}_{k-1}|^2$ . Using the triangle inequality, the Cauchy-Schwarz inequality, and the unitary condition  $\mathbf{\Phi}^H \mathbf{\Phi} = \mathbf{I}$ , the upper bound for the channel strength is derived as [10], [28]:

$$|\mathbf{h}_k^\top (\mathbf{\Phi} - \mathbf{I}) \mathbf{h}_{k-1}|^2 \leq (|\mathbf{h}_k|_2 \|\mathbf{h}_{k-1}\|_2 + |\mathbf{h}_k^\top \mathbf{h}_{k-1}|)^2. \quad (43)$$

Equality holds when

$$\beta \frac{\mathbf{h}_k^*}{\|\mathbf{h}_k\|_2} = \mathbf{\Phi} \frac{\mathbf{h}_{k-1}}{\|\mathbf{h}_{k-1}\|_2}. \quad (44)$$

The structural scattering term in (43) is represented by  $|\mathbf{h}_k^\top \mathbf{h}_{k-1}|^2$ . For LoS channels, the amplitude of the structural scattering term is

$$|\mathbf{h}_k^\top \mathbf{h}_{k-1}| = 1 + \left| \sum_{n=1}^{M-1} e^{jn\pi(\cos \theta_k + \cos \theta_{k-1})} \right|, \quad (45)$$

where  $\theta_k$  and  $\theta_{k-1}$  are the angles of the  $k^{\text{th}}$  and  $(k-1)^{\text{th}}$  users, respectively. The maximum value of the structural scattering term is achieved when  $\theta_k + \theta_{k-1} = \pi$ . Therefore, a sum-rate enhancement is observed at the supplementary angle of FD UE 1 and FD UE 2.

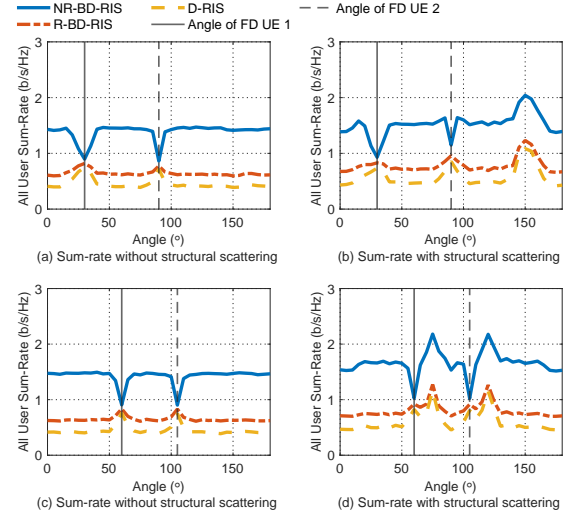


Fig. 10. All-user sum-rates for NR-BD-RIS, R-BD-RIS, and D-RIS with  $M = 16$  RIS elements and  $N = 1$  Tx/Rx antennas. (a), (b): FD UE 1 and UE 2 at  $30^\circ$ ,  $90^\circ$  without/with structural scattering. (c), (d): FD UE 1 and UE 2 at  $60^\circ$ ,  $105^\circ$  without/with structural scattering.

If the locations of FD UE 1 and FD UE 2 are changed to  $60^\circ$  and  $105^\circ$ , respectively, the sum-rate performance is shown in Fig. 10 (c) and (d). The NR-BD-RIS still shows the best sum-rate. When FD UE 3 is not aligned with FD UE 1 or FD UE 2, the NR-BD-RIS outperforms the other two RIS types. Structural scattering also enhances the sum-rate performance at the supplementary angle of FD UE 1 and FD UE 2.

### D. Secure Communication Performance

The proposed secure FD wireless circulator is designed to enforce one-way transmission and prevent eavesdropping among users. In this subsection, we first analyze the received signal power for the  $k^{\text{th}}$  user from other users (*i.e.*,  $\sum i \in \mathcal{K}, i \neq k, k-1$ ). A low received power indicates that the NR-BD-RIS effectively generates nulls in those directions. Consequently, even if an FD user acts as an eavesdropper and probes the direction of other users (*i.e.*,  $\sum i \in \mathcal{K}, i \neq k, k-1$ ), it cannot obtain useful information, therefore ensuring secure communication. Next, we examine the impinging and reflected beam patterns of each FD user to understand how one-way secure transmission and eavesdropping prevention are achieved. Ideally, the impinging beam of each FD user should probe its own direction, while the reflected beam should probe the direction of the next FD user, as illustrated in Fig. 8.

1) *Received Signal Power from Other FD Users*: As shown in Fig. 11, the NR-BD-RIS achieves the lowest received signal power from other users (*i.e.*,  $\sum i \in \mathcal{K}, i \neq k, k-1$ ), effectively suppressing signals from unintended directions. This suppression ensures that no information leakage occurs, even if an FD user attempts to eavesdrop on signals from others. The suppression capability can be further enhanced when multiple antennas are employed at the FD users, providing additional spatial degrees of freedom. In contrast, the R-BD-RIS and D-RIS show higher received signal power from other users (*i.e.*,  $\sum i \in \mathcal{K}, i \neq k, k-1$ ), indicating their limited capability to suppress such signals. The performance gain is due to the

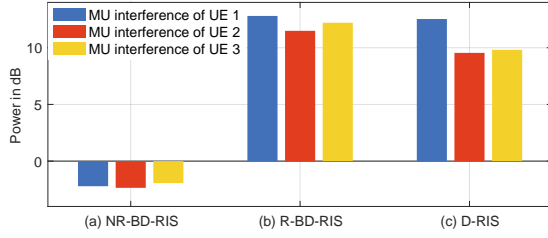


Fig. 11. Received signal power from other  $K - 2$  FD users (*i.e.*,  $\sum i \in \mathcal{K}, i \neq k, k = 1$ ) over noise power for three types of RISs with  $M = 16$  and  $P_t = 40$  dBm. The 3 FD users are positioned at  $60^\circ$ ,  $105^\circ$ , and  $150^\circ$ , respectively. Each FD user is equipped with  $N = 1$  Tx and Rx antenna.

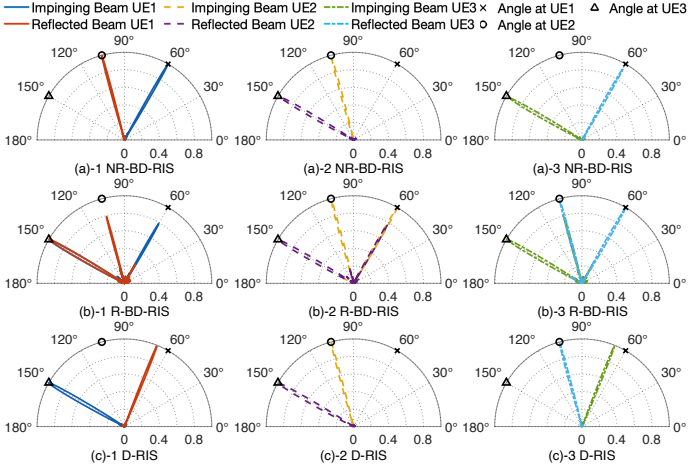


Fig. 12. Impinging and reflected beam patterns for RIS with  $M = 48$  elements without structural scattering. Beam patterns for the three RIS types are shown as follows: (a) NR-BD-RIS, (b) R-BD-RIS, and (c) D-RIS. The first, second, and third columns show the impinging and reflected beam patterns for UE 1, UE 2, and UE 3, respectively. The 3 FD UEs are located at  $60^\circ$ ,  $105^\circ$ , and  $150^\circ$ , respectively. The Tx and Rx antenna numbers are  $N = 1$ .

NR-BD-RIS's ability to break channel reciprocity, enabling greater flexibility in beam control compared to the R-BD-RIS and D-RIS.

2) *Beampattern*: To better understand how PHY secrecy is achieved and why the NR-BD-RIS outperforms the other two RISs, we illustrate the impinging and reflected beampatterns for NR-BD-RIS, R-BD-RIS, and D-RIS. The beampatterns are shown in Fig. 12. The locations of the 3 FD UEs are  $60^\circ$ ,  $105^\circ$ , and  $150^\circ$ , respectively. We set the number of RIS element to  $M = 48$ . Specifically, the optimal directions for each beam are depicted in Fig. 8; the impinging beam of UE 1 should target the direction from UE 1 to the RIS, while the reflected beam of UE 1 should target the direction from the RIS to UE 2. The impinging and reflected beams for UE 2 and UE 3 follow the same principle.

The impinging and reflected beams for the  $k^{\text{th}}$  user without structural scattering are defined as:

$$P_k^{\text{impinging}}(\theta) = |\mathbf{h}_{k+1}^\top \Phi \mathbf{a}(\theta)|^2, \quad P_k^{\text{reflected}}(\theta) = |\mathbf{a}^\top(\theta) \Phi \mathbf{h}_k|^2,$$

where  $\mathbf{a} = \frac{1}{\sqrt{N}}[1, e^{j\pi \cos(\theta)}, \dots, e^{j\pi(N-1) \cos(\theta)}]^\top \in \mathbb{C}^{N \times 1}$  denotes the steering vector, and  $\theta \in [0, 180^\circ]$ . Normalization is applied to ensure the maximum value of the beampattern equals to 1, specifically,

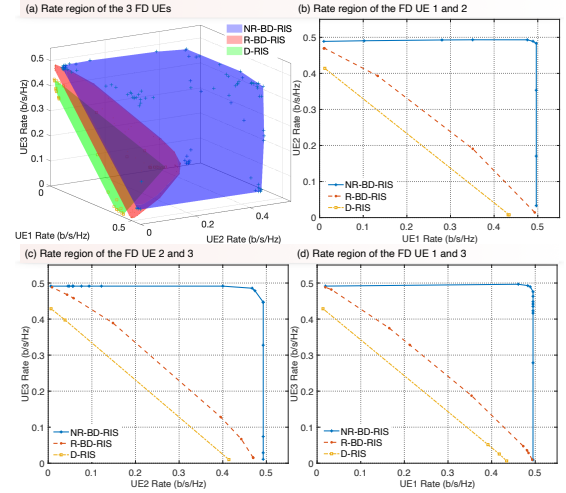


Fig. 13. Sum-rate regions for NR-BD-RIS, R-BD-RIS, and D-RIS with  $M = 16$  without structural scattering. The FD UE locations are  $30^\circ$ ,  $90^\circ$ , and  $150^\circ$ , respectively, with  $N = 1$  TX and RX antennas. (a) Sum-rate region for all 3 FD UEs, (b) Sum-rate region for UE 1 and UE 2, (c) Sum-rate region for UE 2 and UE 3, (d) Sum-rate region for UE 1 and UE 3.

*e.g.*,  $P_k^{\text{impinging}}(\theta)/P_{\text{beam,max}}$ , where  $P_{\text{beam,max}} \triangleq \max \left\{ \max \{P_k^{\text{impinging}}(\theta)\}, \max \{P_k^{\text{reflected}}(\theta)\} \right\}, \forall k \in \mathcal{K}$ .

The first column of Fig. 12 shows the beampatterns for the impinging and reflected beams of UE 1. It can be observed that the impinging beam of UE 1 (*i.e.*, blue beam) correctly probes the direction of UE 1 at  $60^\circ$ , while the reflected beam of UE 1 (*i.e.*, red beam) correctly probes the direction of UE 2 at  $105^\circ$ . In comparison, the R-BD-RIS can probe the desired directions, but the beampattern power is lower than that of the NR-BD-RIS. Part of the impinging beam probes UE 3, which is eavesdropping and can cause information leakage of UE 3. Also, part of the reflected beam probes the direction of UE 3, which can cause information leakage of itself. In addition, the impinging and reflected beams of the D-RIS probe unwanted directions, which can lead to information leakage and eavesdropping.

The second and third columns of Fig. 12 show the impinging and reflected beampatterns of UE 2 and UE 3, respectively. The NR-BD-RIS effectively targets the desired directions, while the R-BD-RIS and D-RIS can only target some of the desired directions. In conclusion, the NR-BD-RIS can achieve one-way secure transmission due to its capability to support multiple beam directions. In contrast, the R-BD-RIS and D-RIS may cause information leakage and eavesdropping due to their limited control of two beam directions. The results of the beampatterns also verify the unique benefit of the NR-BD-RIS in supporting multiple directions, which is reflected in better sum-rate performance compared to the R-BD-RIS and D-RIS, as shown in Fig. 9 and Fig. 10.

#### E. MU Sum-rate Region

Given that the problem formulation  $\mathcal{P}1$  focuses on the weighted sum-rate, we analyze the sum-rate region for the three users. The RIS is configured with  $M = 16$  elements, and TX and RX antennas at each user are set to  $N = 1$ .

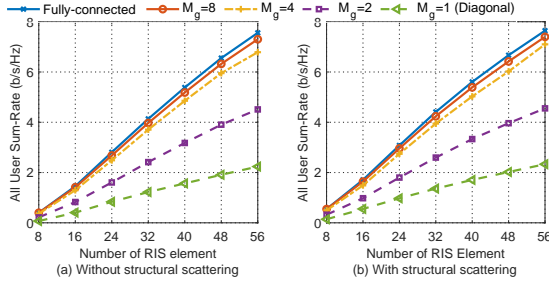


Fig. 14. All-user sum-rates of NR-BD-RIS for varying group sizes  $M_g$ . In (a) and (b), the FD users are positioned at  $60^\circ$ ,  $105^\circ$ , and  $150^\circ$ , respectively. The numbers of Tx and Rx antennas are set to  $N = 1$ .

The users are positioned at  $60^\circ$ ,  $105^\circ$ , and  $150^\circ$ , respectively. To emphasize the benefits of the NR-BD-RIS, the direct links are set to be blocked. The weights  $\alpha_1, \alpha_2$ , and  $\alpha_3$  are varied between 0 and 1, ensuring  $\sum \alpha_k = 1, \forall k \in \mathcal{K}$ . The sum-rate region for all three users is illustrated in Fig. 13 (a). Additionally, Fig. 13 (b), (c), and (d) show the sum-rate regions for UE 1 and UE 2, UE 2 and UE 3, and UE 1 and UE 3, respectively. The results show that the NR-BD-RIS achieves the largest sum-rate region compared to the R-BD-RIS and D-RIS. This is attributed to the NR-BD-RIS's ability to break channel reciprocity and support multiple directions, whereas the R-BD-RIS and D-RIS are limited to one impinging and one reflected direction. Furthermore, the rectangular shape of the NR-BD-RIS's sum-rate region indicates effective interference management, which enables suppression of signals from other users and thus prevents eavesdropping.

#### F. Sum-rates over Group-connected BD-RIS

We investigated the sum-rate performance of the NR-BD-RIS with different group sizes  $M_g$ . The locations of the 3 FD UEs are  $60^\circ$ ,  $105^\circ$ , and  $150^\circ$ , respectively. The direct links are assumed to be blocked. The TX and RX antenna numbers are set to  $N = 1$ . The sum-rates versus the group size are shown in Fig. 14. It can be observed that the sum-rate performance of the NR-BD-RIS increases with the group size. The upper bound is obtained by the fully-connected case, and the lower bound is achieved when the group size is  $M_g = 1$ , which corresponds to the D-RIS. We can also observe that with an increase in the number of RIS element, the gain among different group sizes increases.

#### G. Sum-rates over TX and RX Antennas (MIMO Case)

As detailed in the system model in Section II and the proposed algorithm in Section I, the transmit beamformer and receive combiner are jointly optimized, allowing the performance of MIMO setups to be observed. Fig. 15 illustrates the sum-rate performance with MIMO setups at each FD user for the NR-BD-RIS, R-BD-RIS, and D-RIS as the number of TX and RX antennas varies. We set  $N_t = N_r = N$ . The 3 FD UEs are positioned at  $60^\circ$ ,  $105^\circ$ , and  $150^\circ$ , respectively, with blocked direct links. The results show that the sum-rate performance of the NR-BD-RIS improves with an increasing number of antennas. Moreover, the performance

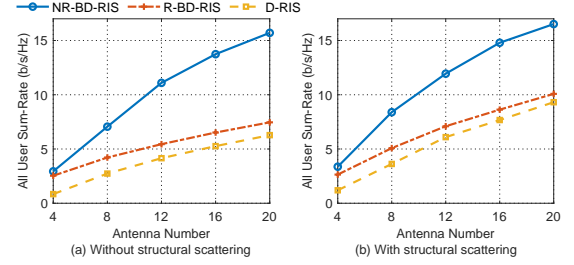


Fig. 15. The all-user sum-rates with MIMO setups (*i.e.*,  $N_t = N_r = N$ ) versus different antenna numbers with  $M = 32$ . The locations of the 3 FD users are  $60^\circ$ ,  $105^\circ$ , and  $150^\circ$ , respectively. The results are shown for (a) without structural scattering and (b) with structural scattering.

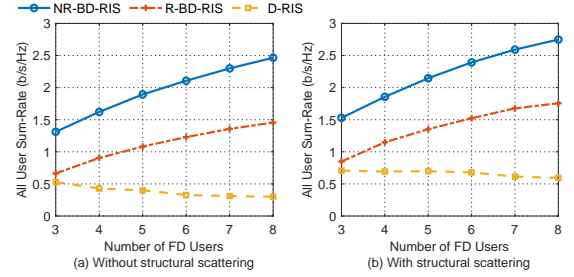


Fig. 16. The all-user sum-rates of NR-BD-RIS, R-BD-RIS, and D-RIS versus the number of FD users  $K$  with  $M = 16$ . The FD users are randomly located in the range of  $(0^\circ, 180^\circ)$ . The numbers of Tx and Rx antennas are set to  $N = 1$ . (a) Without structural scattering, (b) with structural scattering.

gap between the NR-BD-RIS and the other two RIS types widens as the number of antennas increases. Additionally, comparing the case with structural scattering (Fig. 15 (b)) to the case without it (Fig. 15 (a)), the NR-BD-RIS achieves higher sum-rate performance when structural scattering is included. This is because the physics-compliant model, which incorporates structural scattering, leads to higher channel gains [32], thereby enhancing the sum-rate.

#### H. Sum-rates over the Number of FD Users

We further analyze the sum-rate performance of the RISs as the number of FD users  $K$  increases. The FD users are randomly located within the angular range of  $(0^\circ, 180^\circ)$ , and the RIS has  $M = 16$  elements. The results are shown in Fig. 16. Each FD user is equipped with  $N = 1$  TX and RX antennas. The results indicate that the NR-BD-RIS consistently outperforms the R-BD-RIS and D-RIS. Moreover, the sum-rate performance increases as the number of FD users increases. We attribute this to the NR-BD-RIS's capability to support multiple directions, enabling that more FD users can be supported. In contrast, the R-BD-RIS and D-RIS cannot fully support all directions, leading to worse performances. As the number of FD users increases, the sum-rate of the D-RIS decreases due to increased interference among the users. Additionally, when structural scattering is included (cf. Fig. 16 (b)), the NR-BD-RIS achieves higher sum-rate performance compared to the case without structural scattering (cf. Fig. 16 (a)). This enhancement is due to the increased channel gain provided by structural scattering [32].



## VI. CONCLUSION

In this work, we have explored a secure FD wireless circulator system enabled by NR-BD-RIS, facilitating one-way secure transmission and preventing eavesdropping among FD users. The system model considers a physics-compliant channel model that incorporates structural scattering, loop interference, and SI. Structural scattering is essential for accurately modeling the RIS-assisted FD wireless circulator system. We have then formulated the weighted all-user sum-rate maximization problem. To solve this problem, we have proposed an iterative algorithm based on BCD and PDD. The numerical evaluations have shown the advantages of NR-BD-RIS over R-BD-RIS and D-RIS in terms of sum-rate performance due to its capability to break channel reciprocity. We attribute the benefit of the NR-BD-RIS to its ability to support multiple directions, while the R-BD-RIS and D-RIS are limited to one impinging and one reflected direction. The gain of NR-BD-RIS over R-BD-RIS and D-RIS increases with the number of RIS elements, group size, TX and RX antennas, and FD users due to more flexibility. This work has provided insights into the design of NR-BD-RIS for new applications in secure communication.

## REFERENCES

- [1] M. Latva-Aho, K. Leppänen *et al.*, “Key drivers and research challenges for 6G ubiquitous wireless intelligence,” 2019.
- [2] Q. Wu and R. Zhang, “Intelligent reflecting surface enhanced wireless network via joint active and passive beamforming,” *IEEE Trans. Wireless Commun.*, vol. 18, no. 11, pp. 5394–5409, 2019.
- [3] C. Huang, A. Zappone, G. C. Alexandropoulos *et al.*, “Reconfigurable intelligent surfaces for energy efficiency in wireless communication,” *IEEE Trans. Wireless Commun.*, vol. 18, no. 8, pp. 4157–4170, 2019.
- [4] Y. Liu, X. Liu, X. Mu *et al.*, “Reconfigurable intelligent surfaces: Principles and opportunities,” *IEEE Commun. Surveys Tuts.*, vol. 23, no. 3, pp. 1546–1577, 2021.
- [5] H. Guo, Y.-C. Liang, J. Chen *et al.*, “Weighted sum-rate maximization for reconfigurable intelligent surface aided wireless networks,” *IEEE Trans. Wireless Commun.*, vol. 19, no. 5, pp. 3064–3076, 2020.
- [6] 3GPP, “NR; NR repeater radio transmission and reception,” 3rd Generation Partnership Project (3GPP), TS 38.106, Mar. 2023, v.17.4.0. [Online]. Available: <http://www.3gpp.org/ftp/Specs/html-info/38106.htm>.
- [7] Y. Sun, K. An, Y. Zhu *et al.*, “RIS-assisted robust hybrid beamforming against simultaneous jamming and eavesdropping attacks,” *IEEE Trans. Wireless Commun.*, vol. 21, no. 11, pp. 9212–9231, 2022.
- [8] H. Niu, Z. Lin, Z. Chu *et al.*, “Joint beamforming design for secure RIS-assisted IoT networks,” *IEEE Internet Things J.*, vol. 10, no. 2, pp. 1628–1641, 2022.
- [9] Q. Xue, C. Ji, S. Ma *et al.*, “A survey of beam management for mmwave and thz communications towards 6g,” *IEEE Commun. Surveys Tuts.*, vol. 26, no. 3, pp. 1520–1559, 2024.
- [10] S. Shen, B. Clerckx, and R. Murch, “Modeling and architecture design of reconfigurable intelligent surfaces using scattering parameter network analysis,” *IEEE Trans. Wireless Commun.*, vol. 21, no. 2, pp. 1229–1243, Feb. 2022.
- [11] H. Li, S. Shen, M. Nerini *et al.*, “Reconfigurable intelligent surfaces 2.0: Beyond diagonal phase shift matrices,” *IEEE Commun. Mag.*, vol. 62, no. 3, pp. 102–108, Mar. 2024.
- [12] D. M. Pozar, *Microwave engineering: theory and techniques*. Hoboken, NJ, USA: Wiley, 2009.
- [13] M. Nerini, S. Shen, H. Li *et al.*, “Beyond diagonal reconfigurable intelligent surfaces utilizing graph theory: Modeling, architecture design, and optimization,” *IEEE Trans. Wireless Commun.*, 2024.
- [14] M. Nerini and B. Clerckx, “Pareto frontier for the performance-complexity trade-off in beyond diagonal reconfigurable intelligent surfaces,” *IEEE Commun. Lett.*, 2023.
- [15] M. Nerini, S. Shen, and B. Clerckx, “Closed-form global optimization of beyond diagonal reconfigurable intelligent surfaces,” *IEEE Trans. Wireless Commun.*, vol. 23, no. 2, pp. 1037–1051, 2023.
- [16] E. Björnson and Ö. T. Demir, “Capacity maximization for MIMO channels assisted by beyond-diagonal RIS,” *arXiv preprint arXiv:2411.18298*, 2024.
- [17] Q. Li, M. El-Hajjar, I. Hemadeh *et al.*, “Reconfigurable intelligent surfaces relying on non-diagonal phase shift matrices,” *IEEE Trans. Veh. Technol.*, vol. 71, no. 6, pp. 6367–6383, Jun. 2022.
- [18] G. M. Rebeiz and J. B. Muldavin, “RF MEMS switches and switch circuits,” *IEEE Microwave magazine*, vol. 2, no. 4, pp. 59–71, 2001.
- [19] L. Zhang, X. Q. Chen, R. W. Shao *et al.*, “Breaking reciprocity with space-time-coding digital metasurfaces,” *Advanced Materials*, vol. 31, no. 41, p. 1904069, 2019.
- [20] L. Zhang, X. Q. Chen, S. Liu *et al.*, “Space-time-coding digital metasurfaces,” *Nature communications*, vol. 9, no. 1, p. 4334, 2018.
- [21] A. Li, S. Singh, and D. Sevenpiper, “Metasurfaces and their applications,” *Nanophotonics*, vol. 7, no. 6, pp. 989–1011, 2018.
- [22] C. Liaskos, G. G. Pyrialakos, A. Pitilakis *et al.*, “The internet of metamaterial things and their software enablers,” *Int. Telecommun. Union J.*, vol. 1, no. 1, pp. 55–77, 2020.
- [23] F. Rusek, J. Flordelis, E. Bengtsson *et al.*, “Spatially selective reconfigurable intelligent surfaces through element permutation,” in *ICC 2024-IEEE International Conference on Communications*. IEEE, 2024, pp. 5540–5545.
- [24] G. Pan, J. Ye, J. An *et al.*, “Full-duplex enabled intelligent reflecting surface systems: Opportunities and challenges,” *IEEE Wireless Commun.*, vol. 28, no. 3, pp. 122–129, Jun. 2021.
- [25] H. Wang, Z. Han, and A. L. Swindlehurst, “Channel reciprocity attacks using intelligent surfaces with non-diagonal phase shifts,” *IEEE Open J. of the Comm. Society.*, 2024.
- [26] J. Xu, H. Wang, R. Liu *et al.*, “Non-reciprocal reconfigurable intelligent surfaces,” *arXiv preprint arXiv:2411.15617*, 2024.
- [27] H. Li and B. Clerckx, “Non-reciprocal beyond diagonal RIS: Multiport network models and performance benefits in full-duplex systems,” Nov. 2024, arXiv:2411.04370.
- [28] Z. Liu, H. Li, and B. Clerckx, “Non-reciprocal BD-RIS in full-duplex communications: A perspective on sum-rate maximization,” *arXiv preprint arXiv:2411.18523*, 2024.
- [29] H. Li, S. Shen, Y. Zhang *et al.*, “Channel estimation and beamforming for beyond diagonal reconfigurable intelligent surfaces,” *IEEE Trans. Sig. Proc.*, vol. 72, pp. 3318–3332, 2024.
- [30] R. C. Hansen, “Relationships between antennas as scatterers and as radiators,” *Proc. IEEE*, vol. 77, no. 5, pp. 659–662, 1989.
- [31] A. Abrardo, A. Toccafondi, and M. Di Renzo, “Design of reconfigurable intelligent surfaces by using s-parameter multiport network theory—optimization and full-wave validation,” *IEEE Trans. Wireless Commun.*, 2024.
- [32] M. Nerini, G. Gradoni, and B. Clerckx, “Physics-compliant modeling and scaling laws of multi-RIS aided MIMO systems,” *arXiv preprint arXiv:2411.06309*, 2024.
- [33] M. Nerini, S. Shen, H. Li *et al.*, “A universal framework for multiport network analysis of reconfigurable intelligent surfaces,” *IEEE Trans. Wireless Commun.*, 2024.
- [34] K. Shen and W. Yu, “Fractional programming for communication systems—Part I: Power control and beamforming,” *IEEE Trans. Sig. Proc.*, vol. 66, no. 10, pp. 2616–2630, 2018.
- [35] D. P. Bertsekas, “Nonlinear programming,” *J. Oper. Res. Soc.*, vol. 48, no. 3, pp. 334–334, 1997.
- [36] Q. Shi and M. Hong, “Penalty dual decomposition method for non-smooth nonconvex optimization—Part I: Algorithms and convergence analysis,” *IEEE Trans. Sig. Proc.*, vol. 68, pp. 4108–4122, 2020.
- [37] Y. Zhou, Y. Liu, H. Li *et al.*, “Optimizing power consumption, energy efficiency and sum-rate using beyond diagonal RIS—a unified approach,” *IEEE Trans. Wireless Commun.*, 2023.
- [38] W. Gibson, “On the least-squares orthogonalization of an oblique transformation,” *Psychometrika*, vol. 27, no. 2, pp. 193–195, 1962.
- [39] J. H. Manton, “Optimization algorithms exploiting unitary constraints,” *IEEE Trans. Sig. Proc.*, vol. 50, no. 3, pp. 635–650, 2002.
- [40] G. H. Golub and C. F. Van Loan, *Matrix computations*, Johns Hopkins University Press, 3rd edition, 1996.
- [41] E. Everett, C. Shepard, L. Zhong *et al.*, “SoftNull: Many-antenna full-duplex wireless via digital beamforming,” *IEEE Trans. Wireless Commun.*, vol. 15, no. 12, pp. 8077–8092, 2016.
- [42] B. Debaillie, D.-J. van den Broek, C. Lavin *et al.*, “Analog/RF solutions enabling compact full-duplex radios,” *IEEE J. Sel. Areas Commun.*, vol. 32, no. 9, pp. 1662–1673, 2014.
- [43] Z. Liu, A. Bhandari, and B. Clerckx, “Full-duplex beyond self-interference: The unlimited sensing way,” *IEEE Commun. Lett.*, 2024.